Materials Today Advances 30 (2026) 100774

Contents lists available at ScienceDirect

Materials Today Advances

journal homepage: www.journals.elsevier.com/materials-today-advances/

Ferrocene-loaded glycerogel dressing for reactive oxygen species-modulated active wound healing

Jiwon Kang [a,b,1], Sohyun Yu [a,c,1], Jisu Kim [a,c,1], Seongwoo Yang [d,e,1], Won Il Choi [a], Jinhan Cho [b], Jeonghun Kim [e,**], Daekyung Sung [a,***], Byoung Soo Kim [a,*]

[a] Center for Bio-Healthcare Materials, Bio-Convergence Materials R&D Division, Korea Institute of Ceramic Engineering and Technology, Chungbuk, 28160, Republic of Korea
[b] School of Chemical and Biomolecular Engineering, Korea University, 145, Anam-ro, Seongbuk-gu, Seoul, 02841, Republic of Korea
[c] School of Chemical and Biomolecular Engineering, Yonsei University, 50 Yonsei-ro, Seodaemun-gu, Seoul, 03722, Republic of Korea
[d] Department of Medical Device Management and Research, SAIHST, Sungkyunkwan University, Seoul, 06355, Republic of Korea
[e] Biomedical Engineering Research Center, Samsung Medical Center, Seoul, 06351, Republic of Korea

ARTICLE INFO

Keywords:
Wound dressing
Bioadhesive hydrogel
Ferrocene-based polymer
Reactive oxygen species-responsive nanoparticle
Tough hydrogel

ABSTRACT

Chronic and complex wounds remain a major clinical challenge owing to persistent oxidative stress, impaired tissue regeneration, and insufficient therapeutic efficacy of conventional wound dressings. Therefore, in this study, we aimed to investigate the wound-healing efficacy of a novel multifunctional wound dressing that integrates a mechanically robust bioadhesive glycerogel matrix with a reactive oxygen species (ROS)-responsive drug nanocarrier. Specifically, a resilient glycerogel was obtained from a single acrylamide monomer formulation with enhanced polymer entanglement and solvent exchange capacity, inducing long-term hydration and strong tissue adhesion. Ferrocene-based polymer nanoparticles encapsulating *Centella asiatica* enabled on-demand antioxidant release in response to elevated ROS levels, thereby dynamically modulating the wound microenvironment. Notably, this multifunctional dressing effectively maintained a moist wound environment, promoted healing through controlled redox-triggered drug release at the wound site, and exhibited excellent cytocompatibility. Moreover, it promoted fibroblast proliferation and migration as well as ROS scavenging *in vitro*. Additionally, this dressing accelerated wound closure, enhanced re-epithelialization, reduced inflammation, and guided collagen alignment toward a skin-like architecture in vivo. In conclusion, this bioadhesive, ROS-responsive glycerogel dressing represents a versatile therapeutic platform that actively engages in pathological wound environments, showing superior effects compared with conventional hydrogel-based dressings.

1. Introduction

Wound dressings have undergone a paradigm shift from passive protective barriers to active therapeutic platforms designed to regulate the wound microenvironment and promote tissue regeneration [1,2]. Conventional dressings, such as gauze, foams, and hydrocolloids, primarily serve to protect the wound and manage exudate, supporting autolytic debridement by maintaining a moist interface [3,4]. However, in complex wounds associated with chronic pathologies or extensive tissue loss, the endogenous regenerative response is often impaired. A key contributing factor is the dysregulation of reactive oxygen species (ROS). While transient ROS levels are essential for host defense and cellular signaling, excessive and persistent ROS accumulation amplifies inflammation, degrades extracellular matrix components, and delays tissue regeneration [5–7]. This has driven increasing interest in bioactive dressings that not only maintain hydration but also actively modulate oxidative stress.

Hydrogels are promising candidates for wound dressings due to their high water content and tissue-like properties, which support a hydrated interface and facilitate healing [8–10]. However, conventional hydrogels are often mechanically fragile and highly susceptible to dehydration under ambient conditions, limiting their functional longevity [11,12].

* Corresponding author.
** Corresponding author.
*** Corresponding author.
E-mail addresses: jeonghun0113.kim@samsung.com (J. Kim), dksung@kicet.re.kr (D. Sung), bskim@kicet.re.kr (B.S. Kim).
[1] These authors contributed equally.

https://doi.org/10.1016/j.mtadv.2026.100774
Received 6 December 2025; Received in revised form 25 March 2026; Accepted 6 April 2026

To address dehydration, solvent-exchanged hydrogels incorporating hygroscopic solvents such as glycerol have been developed to enhance moisture retention and environmental stability [13]. These glycerogel systems exhibit improved resistance to drying and sustain hydration during wound contact. Nevertheless, their application as active drug delivery matrices, particularly for responsive therapeutic systems, remains underexplored.

To improve mechanical robustness, tough hydrogel systems based on double-network (DN) architectures have been extensively studied [14–16]. In such systems, a covalently crosslinked primary network provides structural integrity, while a secondary ionically crosslinked network dissipates energy under deformation. However, the presence of ionic domains can impose limitations for drug delivery applications [17,18]. Electrostatic interactions between the network and encapsulated agents may hinder nanoparticle mobility, restrict diffusion, and lead to delayed or unpredictable release profiles. Achieving high mechanical toughness without introducing such ionic constraints therefore remains a critical design challenge.

To address oxidative imbalance, ROS-responsive drug delivery systems have been widely investigated. Among various approaches, ferrocene-based materials are particularly attractive due to their reversible redox behavior, enabling efficient structural transformation and controlled drug release under oxidative conditions [19,20]. Compared to other ROS-responsive motifs, such as boronic esters or thioethers, ferrocene systems often exhibit more rapid and robust responsiveness. In addition, ferrocene-based carriers facilitate the incorporation of hydrophobic therapeutic agents into hydrophilic matrices. This is particularly relevant for bioactive compounds such as *Centella asiatica* (CA), which promotes collagen synthesis, enhances fibroblast proliferation, and exerts anti-inflammatory effects [21]. However, effective delivery of CA in a controlled and responsive manner remains a challenge in conventional formulations.

To address these challenges, we present a single-monomer-based tough glycerogel integrated with ROS-responsive ferrocene-functionalized nanoparticles. By tuning the monomer-to-crosslinker ratio, polymer chain entanglement serves as the primary energy dissipation mechanism, enabling mechanical toughness without introducing ionic interactions that could hinder nanoparticle diffusion (Fig. 1a). A solvent-exchange strategy is employed to partially replace water with glycerol, forming a non-drying glycerogel with enhanced moisture retention [22,23]. Ferrocene-functionalized nanoparticles are incorporated as a redox-responsive module to enable ROS-triggered release of encapsulated therapeutics (Fig. 1b), and *Centella asiatica* is loaded as a model payload to evaluate the combined effects of oxidative stress modulation and pro-regenerative activity. This integrated platform is designed to simultaneously regulate oxidative stress, maintain a stable hydrated environment, and promote tissue regeneration (Fig. 1c). The multifunctional performance of the system is systematically evaluated through mechanical characterization, *in vitro* release studies, and in vivo wound healing assessments.

2. Results and discussion

2.1. Synthesis and characterization of ferrocene-based polymer

A ferrocene-based polymer (FP) was synthesized via the random radical polymerization of ferrocenylmethyl methacrylate (FMMA), methacrylate (MA), and polyethylene glycol MA (PEGMA) (Fig. 2a). Given the hydrophobic nature of CA, we investigated its encapsulation efficiency (LE) by comparing two polymer compositions: a standard FP and an FP functionalized with PEG, referred to as FP-PEG. PEG was added to improve the hydrophilicity and dispersion stability of the

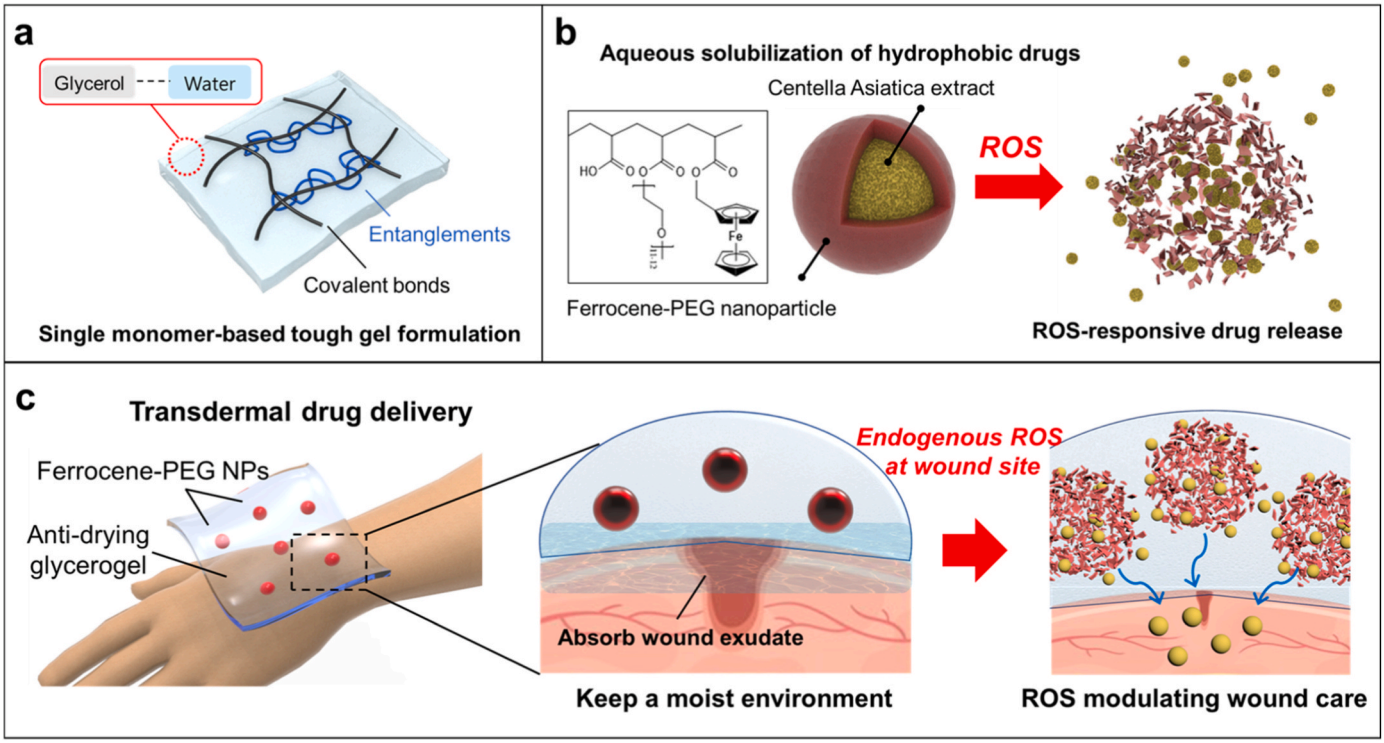

Fig. 1. Schematic illustration of the multifunctional glycerogel wound dressing and its reactive oxygen species (ROS)-responsive drug release mechanism. (a) Structure of the moisture-retaining glycerogel network. Hygroscopic glycerol reduces water loss, and dense polymer entanglements contribute to mechanical robustness. (b) Structure of *Centella asiatica* (CA)-loaded ferrocene–polyethylene glycol (PEG) nanoparticles (NPs) (CA@FP-PEG NPs) and their ROS-triggered drug release mechanism. Oxidation of the ferrocene core under elevated ROS induces NP disassembly and controlled CA release. (c) Application of the glycerogel-CA@FP-PEG NP patch on skin. The glycerogel dressing maintains a moist environment, absorbs wound exudate, and delivers antioxidant therapeutics in response to local ROS levels.

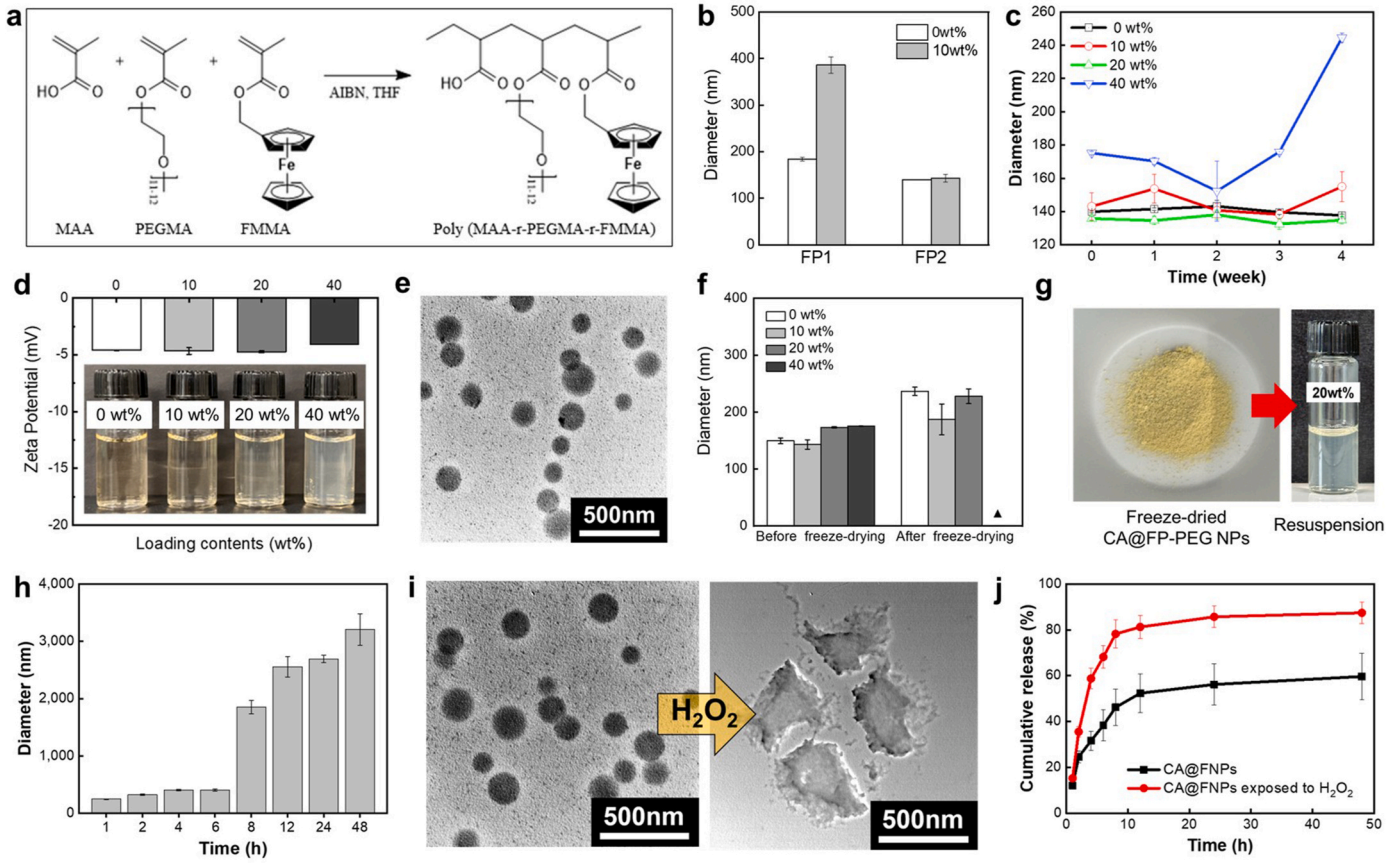

Fig. 2. Synthesis, characterization, and reactive oxygen species (ROS) responsiveness of CA@FP-PEG NPs. (a) Synthetic scheme of the ferrocene-containing random copolymer poly(MA-r-PEGMA-r-FMMA) used for NP formation. (b) Hydrodynamic diameters of NPs from FP or FP-PEG, before and after encapsulation of 10 wt% *Centella asiatica* (CA). (c) Size and storage stability of CA@FP–PEG NPs with varying CA loading ratios (0 – 40 wt%). (d) Zeta potential values of CA@FP-PEG NPs as a function of CA loading. Inset images show the visual appearance of NP dispersions. (e) TEM image of CA@FP-PEG NPs containing 20 wt% CA. (f) Hydrodynamic diameters of CA@FP-PEG NPs with different CA loading ratios (0 – 40 wt%) before and after freeze-drying. (g) Photographic images of freeze-dried CA@FP-PEG NPs (20 wt% CA) and their redispersion after rehydration. (h) ROS responsiveness of CA@FP-PEG NPs evaluated by changes in hydrodynamic diameter over time upon exposure to 200 mM H_2O_2. (i) TEM images of CA@FP-PEG NPs before (left) and after (right) exposure to 200 mM H_2O_2 for 6 h, showing ROS-triggered structural disruption. (j) Cumulative release profile of CA from CA@FP-PEG NPs in PBS (pH 7.4, 37 °C) with 200 mM H_2O_2.

polymer in aqueous environments while maintaining efficient CA loading. Additionally, the chemical structures and compositions of the synthesized FP and FP-PEG were confirmed using proton nuclear magnetic resonance (^{1}H NMR) spectroscopy and gel permeation chromatography (GPC) (Fig. S1 and Table S1). Notably, the successful polymerization of FMMA, MA, and PEGMA was confirmed by the appearance of characteristic polymer peaks at 12.3, 4.1, and 3.5 ppm in the ^{1}H NMR spectrum, corresponding to protons in the MA, FMMA, and PEGMA blocks, respectively, consistent with a previous report [24]. Negligible intensity was observed for the monomer-specific peaks near 5.38 and 271 ppm, confirming complete polymerization. Additionally, the molecular weight distributions of FP and FP-PEG were analyzed using GPC (Table S1). Notably, the weight-average molecular weight (Mw) and number-average molecular weight (Mn) ratios (polydispersity index, PDI) were 1.60 for FP and 1.72 for FP-PEG, indicating a relatively uniform chain length distribution. Additionally, the increased PDI of FP-PEG suggests a broader molecular weight distribution due to the incorporation of PEG, which may enhance drug encapsulation properties and aqueous dispersibility.

2.2. Preparation and characterization of CA-loaded FP-PEG NPs

CA-loaded FP-PEG NPs (CA@FP-PEG NPs) were synthesized using a nanoprecipitation method, with both FP and FP-PEG as the encapsulating polymers. For the initial screening, CA was loaded at 10 wt% relative to the polymer. Nanoparticle stability was evaluated by monitoring the hydrodynamic diameter using dynamic light scattering (DLS). FP and FP-PEG NPs without CA exhibited average hydrodynamic diameters of approximately 200 and 135 nm, respectively (Fig. 2b). The smaller size of FP-PEG NPs was likely attributed to the presence of PEG chains, which promoted the formation of denser and more compact structures owing to enhanced hydrophilicity and flexible chain packing during self-assembly [25,26]. However, the particle size nearly doubled following the loading of CA into FP NPs (CA@FP NPs), and the suspension appeared visibly opaque (Fig. 2b and Fig. S2), suggesting incomplete encapsulation and dispersion of free CA in the solution. In contrast, CA@FP-PEG NPs retained a size similar to that of unloaded FP-PEG NPs, with no notable size change observed (Fig. 2b). Additionally, the resulting solution became transparent after encapsulation, indicating improved solubility and efficient CA encapsulation within the FP-PEG particles (Fig. S2).

To determine the optimal drug-loading capacity (LC) of FP-PEG NPs, we prepared a series of CA@FP-PEG NPs with CA loadings of 0, 10, 20, and 40 wt% relative to the polymer (Fig. 2c). All formulations initially exhibited stable nanoparticle formation, with the particles remaining well-formed even at 40 wt% CA loading (only a slight increase in size was observed). Except for the 40 wt% CA formulation, all nanoparticle formulations demonstrated exceptional stability over the 28-day period. Notably, the 20 wt% CA@FP-PEG NP formulation exhibited the highest stability. DLS measurements confirmed that the hydrodynamic

diameters remained relatively constant, with no significant fluctuations over time (Fig. 2c). Furthermore, the size distribution remained highly uniform, as indicated by a PDI < 0.10 (Fig. S3), suggesting a well-dispersed and homogeneous nanoparticle population. In contrast, the 40 wt% CA@FP-PEG NPs exhibited a marked increase in hydrodynamic diameter and a progressive decline in colloidal stability in the third and fourth weeks. Based on these results, the maximum stable drug loading was determined to be 20 wt%. Importantly, the stability of CA@FP-PEG NPs was corroborated by zeta potential measurements, which indicated that all formulations had an adequate surface charge to maintain colloidal stability at the time of synthesis (Fig. 2d). Transmission electron microscopy (TEM) confirmed that the 20 wt% formulation exhibited uniform particle morphology and maintained a consistent size distribution (Fig. 2e).

To assess the feasibility of long-term storage and redispersibility for potential commercial applications, CA@FP-PEG NP formulations with varying CA concentrations (0–40 wt%) were subjected to lyophilization without cryoprotectants, such as trehalose or glucose. For consistency, the particle size data shown here were obtained from the same experimental batch used for the initial size characterization. After resuspension, the 20 wt% formulation was readily redispersed into a clear solution with no noticeable change in particle size, indicating excellent lyophilization tolerance (Fig. 2f and g). Overall, these results suggest that CA@FP-PEG NPs with 20 wt% loading can be stably stored in dried form and reconstituted without compromising their colloidal stability, making them more suitable for long-term storage and practical use.

2.3. ROS responsiveness of CA@FP-PEG NPs

The ROS sensitivity of CA@FP-PEG NPs was evaluated by monitoring changes in particle size and tracking the release profile of encapsulated CA using high-performance liquid chromatography (HPLC). Hydrogen peroxide (H_2O_2) was used as a model ROS agent at a concentration of 200 mM to simulate the elevated oxidative conditions typically found in wound environments [27,28]. After exposure to H_2O_2 for 6 h, the hydrodynamic diameter of CA@FP-PEG NPs increased to approximately 480 nm (Fig. 2h). Additionally, the NPs swelled further to approximately 1750 nm after continuous oxidation for 8 h. TEM was performed to visualize the ROS-responsive morphological transformation of

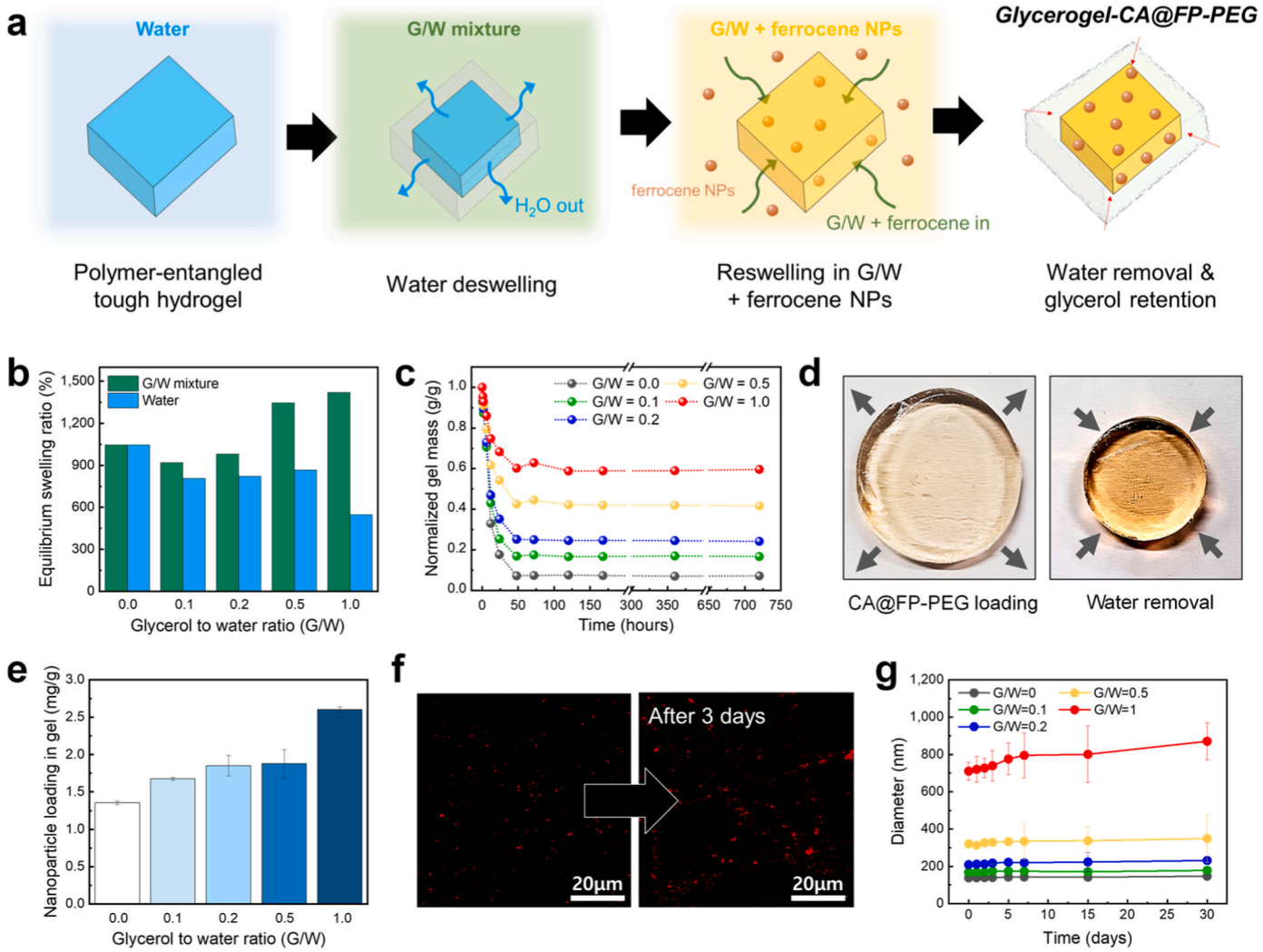

Fig. 3. Fabrication and characterization of glycerogel-CA@FP-PEG NPs. (a) Schematic illustration of the fabrication process of glycerogel-CA@FP-PEG NPs. (b) Equilibrium swelling ratio (ESR) of glycerogels prepared with different glycerol-to-water (G/W) ratios, with moisture content quantified by thermogravimetric analysis (TGA). (c) Water retention profiles of glycerogel-CA@FP-PEG NPs with varying G/W ratios over 30 days under ambient conditions. (d) Photographic images showing the loading of CA@FP-PEG NPs into the glycerogel and the appearance after excess water removal for 3 days. (e) Quantification of CA@FP–PEG NP loading capacity per gram of glycerogel at different G/W ratios. (f) Confocal fluorescence microscopy images of Nile Red-loaded FP-PEG NPs, demonstrating uniform distribution within the glycerogel (G/W = 0.2), before and after 3 days of exposure to open air. (g) Colloidal stability of CA@FP–PEG NPs in dispersion with varying G/W ratios over a 30-day period. (For interpretation of the references to colour in this figure legend, the reader is referred to the Web version of this article.)

CA@FP-PEG NPs (Fig. 2i). Substantial structural disruption was observed after 6 h of H_2O_2 exposure. This expansion is attributed to the rapid diffusion of H_2O_2 through the carboxyl-functionalized polymer shell, which oxidizes the ferrocene core, leading to structural swelling and nanoparticle destabilization. This progressive increase in size enables on-demand drug release tailored to the oxidative stress levels in the wound microenvironment.

To further elucidate ROS-triggered drug release behavior, we investigated the release kinetics of CA under oxidative conditions (Fig. 2j). In the absence of H_2O_2, CA@FP-PEG NPs exhibited a sustained release profile, with approximately 60% of the encapsulated CA diffusing into the biological buffer over 8 h at 37 °C. However, the release rate markedly increased after exposure to 200 mM H_2O_2, with approximately 80% of the CA released within 12 h. This accelerated drug release under oxidative stress suggests that ferrocene oxidation plays a critical role in modulating drug release, thereby enabling a responsive delivery mechanism in ROS-rich environments.

2.4. Preparation of glycerogel and integration with CA@FP-PEG NPs

A mechanically robust, non-drying, and adhesive glycerogel dressing was fabricated by synthesizing a polyacrylamide hydrogel, followed by solvent exchange with a water–glycerol mixture (Fig. 3a and Fig. S4). Specifically, the resilient polyacrylamide hydrogel was polymerized at a crosslinker-to-monomer molar ratio of 1:10,800, as previously reported [29]. After polymerization, the hydrogel was incubated in glycerol–-water mixtures for 5 d, allowing partial solvent replacement. Thereafter, excess water was removed, resulting in slight shrinkage caused by the loss of unbound water and the evaporation of glycerol. The CA@FP-PEG NPs were introduced into the glycerogel by incubating the gel matrix in a CA@FP-PEG NP dispersion in water. Following another round of excess water removal, a resilient, non-drying, and adhesive glycerogel-based wound dressing was successfully obtained (Fig. 3a and Fig. S4).

2.5. Characterization of glycerogel-CA@FP-PEG NPs

As swelling capacity directly affects the loading efficiency of CA@FP-PEG NPs and the glycerol content determines the non-drying properties, we examined the equilibrium swelling ratio (ESR) of the glycerogel under varying glycerol-to-water (G/W) incubation conditions (0, 0.1, 0.2, 0.5, and 1.0). Thermogravimetric analysis (TGA) was used to estimate the water and glycerol contents after equilibration. As the G/W ratio increased, the ESR increased accordingly, but a reduction in the absolute water content was observed (Fig. 3b and Fig. S5).

The water retention capacity of the glycerogel dressing was assessed by monitoring changes in sample mass under ambient conditions for more than 1 month (Fig. 3c). Notably, the observed mass loss was primarily attributed to water evaporation. For the control hydrogel (G/W = 0), which contained no glycerol, approximately 80% of the water evaporated within 24 h, leading to complete dehydration and rigid deformation within 48 h. In contrast, all glycerogel samples prepared in glycerol-water mixtures remained moist throughout the 30-day period. Most of the excess water was removed within the first 48 h, after which the sample mass remained nearly constant, indicating that dehydration had reached equilibrium. Water retention improved with increasing glycerol content, highlighting the hygroscopic nature of glycerol. Specifically, glycerogel dressings prepared with G/W ratios of 0.1, 0.2, 0.5, and 1.0 retained 83%, 76%, 58%, and 48% of their initial mass, respectively. Consistent with these quantitative results, photographic observations showed that the glycerogel maintained a hydrated appearance even after loading with CA@FP–PEG NPs and removal of excess water for 3 days (Fig. 3d). Collectively, these results confirm that glycerol effectively prevented complete drying and ensured prolonged hydration of the dressings.

The loading efficiency of CA@FP-PEG NPs within the glycerogel matrix was quantified at different G/W ratios (Fig. 3e). To determine the amount of CA@FP-PEG NPs incorporated into the glycerogel, the concentration of CA@FP-PEG NPs in the incubation solution was measured before and after introduction. All CA@FP-PEG NPs solutions were prepared at a fixed concentration of 0.5 g/L to ensure consistency, and the total amount of solution absorbed by the glycerogel was estimated by calculating the weight difference before and after swelling. The residual CA@FP-PEG NP concentration in the remaining solution was measured at 285 nm to quantify loading efficiency using ultraviolet-visible (UV-Vis) spectroscopy. Notably, the loading amount of CA@FP-PEG NPs increased with increasing G/W ratios during glycerogel incubation (Fig. 3e). This trend closely followed the ESR of the glycerogels at different G/W compositions, with the highest loading efficiency observed at a G/W ratio of 1.0 (Fig. 3b). To confirm the successful incorporation of CA@FP-PEG NPs into the glycerogel matrix, Nile Red (NR)-loaded FP-PEG NPs were used as fluorescent tracers. Confocal microscopy revealed that the FP-PEG NPs were uniformly distributed throughout the glycerogel and remained stably embedded even the removal of excess water, indicating strong retention within the glycerogel matrix (Fig. 3f). Overall, these results indicate that glycerogel swelling directly affects the capacity for nanoparticle uptake, with higher swelling leading to an enhanced drug-loading efficiency.

The stability of CA@FP-PEG NPs within the glycerol mixture system was assessed by monitoring particle size variations over time using DLS. The structural integrity of CA@FP-PEG NPs in solution was evaluated by tracking the changes in hydrodynamic diameter, as particle swelling or aggregation typically indicates destabilization (Fig. 3g). Consistent with the original particle size, the nanoparticle size remained below 200 nm when incubated in solutions with G/W ratios of 0, 0.1, and 0.2, confirming structural stability. In contrast, a rapid increase in hydrodynamic diameter was observed at higher G/W ratios (0.5 and 1.0), indicating reduced nanoparticle stability. This phenomenon is attributed to glycerol diffusion into the FP-PEG polymer network, which disrupts the structural integrity of the NPs and leads to particle swelling or collapse, followed by partial oxidation or aggregation [30]. Considering the balance between drug-loading efficiency, nanoparticle stability, and non-drying properties, a G/W ratio of 0.2 was identified as optimal for glycerogel-CA@FP-PEG NP formulation.

2.6. Mechanical and adhesive properties of glycerogel-CA@FP-PEG NPs

Mechanical robustness and interfacial adhesion of wound dressings are critical parameters that directly affect their usability and therapeutic effectiveness. To evaluate these properties, we investigated the tensile strength and adhesive performance of glycerogels and CA@FP-PEG NPs fabricated with a G/W ratio of 0.2. Under ambient conditions, both the pristine glycerogel and glycerogel-CA@FP-PEG NPs exhibited high stretchability, with elongations at break exceeding 700 and 900%, respectively (Fig. 4a). Importantly, the addition of CA@FP-PEG NPs further enhanced the mechanical stiffness of the hydrogel matrix, increasing the ultimate tensile strength to 386.5 kPa and Young's modulus to 2.0 kPa, approximately 1.3-fold higher than that of the glycerogel (Fig. 4a and Fig. S6). This mechanical enhancement likely results from the formation of intermolecular hydrogen bonds between the amide groups of polyacrylamide and the ether groups of NPs and the polyacrylamide network, which reinforces the internal stress distribution within the gel [31,32].

To assess tissue adhesion, we tested both the glycerogel and glycerogel-CA@FP-PEG NPs on hydrated porcine skin, which closely mimics the mechanical and biological properties of human skin (Fig. 4b and c). Unlike conventional polyacrylamide-based hydrogels, which are typically nonadhesive, glycerogel systems exhibit intrinsic adhesive behavior without the need for chemical modification or adhesive additives. Lap shear and tensile adhesion tests confirmed that the adhesion strength was strongly affected by the G/W ratio used during gel preparation (Fig. 4b and c). A lower glycerol content (lower G/W ratio)

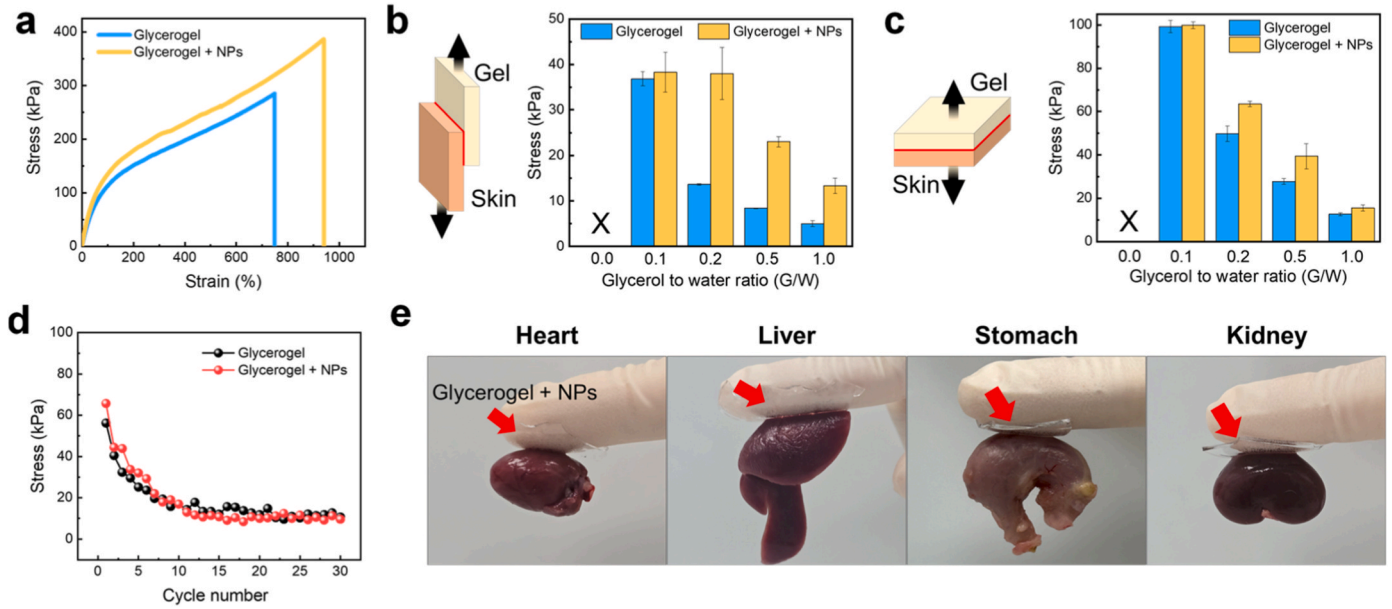

Fig. 4. Mechanical and adhesive properties of glycerogel–CA@FP–PEG NPs. (a) Representative stress-strain curves of glycerogel and glycerogel-CA@FP-PEG NPs (G/W = 0.2). (b) Lap shear and (c) tensile adhesion strength between gels and hydrated porcine skin. (d) Cyclic adhesion performances of glycerogel and glycerogel-CA@FP-PEG NPs (G/W = 0.2) on porcine skin over 30 attach–detach cycles. (e) Photographs demonstrating adhesion of glycerogel–CA@FP–PEG NPs to various organs of Sprague–Dawley rats.

resulted in a higher adhesive strength. Moreover, the incorporation of CA@FP-PEG NPs further increased the adhesive performance across all compositions, indicating their potential role in enhancing interfacial interactions.

This unexpected adhesiveness is attributed to partial dehydration during the excess water removal stage, which locally concentrates functional groups such as amide and hydroxyl moieties at the gel–skin interface (Fig. S7). Additionally, thinning of the interfacial water-bound layer due to evaporation reduces the hydration barrier between the gel and substrate, thereby facilitating closer molecular contact. Another advantage of this system is the tunability of the adhesive strength via glycerol content modulation. Higher glycerol contents resulted in lower adhesion but superior moisture retention, whereas lower glycerol levels enhanced adhesion. This tunability is particularly important in clinical settings where different wound types require tailored adhesion levels.

In cyclic adhesion tests on porcine skin, the initial adhesion strengths of glycerogel and glycerogel-CA@FP-PEG NPs at G/W of 0.2 were 56.2 and 65.7 kPa, respectively (Fig. 4d). However, both samples exhibited a gradual reduction in strength after 30 adhesion–removal cycles, retaining only 15–18% of their initial values, likely due to partial detachment or damage to the porcine epidermis caused by repeated peeling. Despite this decline, adhesion performance remained comparable to that of several commercially available tissue sealants, including cyanoacrylate-based formulations (vetbond and histoacryl) and hydrogel-based adhesives (fibrin glue), which typically exhibit adhesion strengths below 10 kPa [33,34]. For comparison, gel-to-gel adhesion tests were also conducted. Glycerogel and glycerogel-CA@FP-PEG NPs maintained stable gel-to-gel adhesion for at least 30 attachment–detachment cycles. Notably, the dressings retained approximately 76–78% of their initial strength after repeated cycling (Fig. S8), demonstrating better durability under synthetic and non-biological conditions. Despite this decline, the dressing still maintained sufficient adhesive strength and readily adhered to various rat organs, highlighting its robust wet-tissue adhesion and potential applicability to diverse wound sites (Fig. 4e).

2.7. Cytocompatibility and ROS scavenging ability of glycerogel-CA@FP-PEG NPs

To evaluate the biocompatibility and antioxidant potential of the glycerogel-CA@FP-PEG NP system, we systematically investigated its cytotoxicity and ROS-scavenging ability *in vitro*. Cell Counting Kit (CCK-8) assay was performed to assess the cytotoxicity of CA@FP-PEG NPs in NIH3T3 fibroblasts across a concentration range of 0 – 200 μg mL^{-1} (gel-to-medium dosing). Cell viability remained above 95% at concentrations of up to 100 μg mL^{-1}, indicating negligible cytotoxicity within the concentration range relevant for therapeutic applications (Fig. 5a). Based on these results, 100 μg/mL was selected as the optimal concentration for subsequent loading into the glycerogel matrix.

To confirm the cytocompatibility of the individual components and the final formulation, NIH3T3 fibroblasts were treated with glycerogel, CA@FP–PEG NPs, and glycerogel–CA@FP–PEG NPs. A glycerogel–CA group was not included because free CA is poorly soluble and dispersible in the glycerogel matrix, which could lead to heterogeneous distribution and unreliable biological responses. All treatment groups maintained cell viability above 90%, demonstrating that both the matrix and nanoparticle components were nontoxic and suitable for biomedical use (Fig. 5b). Additionally, the antioxidant activity of the formulation was investigated using a DPPH radical scavenging assay. Three formulations were compared: glycerogel, glycerogel-FP-PEG NPs (without CA), and (glycerogel-CA@FP-PEG NPs.

Although all samples showed similar activity within the first 6 h, only the CA-loaded group exhibited a significant increase in DPPH scavenging activity after 6 h, confirming that the encapsulated CA retained its ROS-neutralizing functionality within the nanoparticle system (Fig. 5c).

In NIH3T3 cells subjected to H_2O_2-induced oxidative stress, intracellular ROS levels were monitored using the H2DCFDA fluorescence assay. Cells treated with glycerogel–CA@FP–PEG NPs exhibited an 82% reduction in ROS levels at 8 h post-treatment compared with the H_2O_2-only control (Fig. 5d and e), indicating effective intracellular ROS neutralization. Consistently, the representative fluorescence images in Fig. 5e showed markedly weaker intracellular fluorescence signals after treatment, confirming the reduction of ROS at the cellular level.

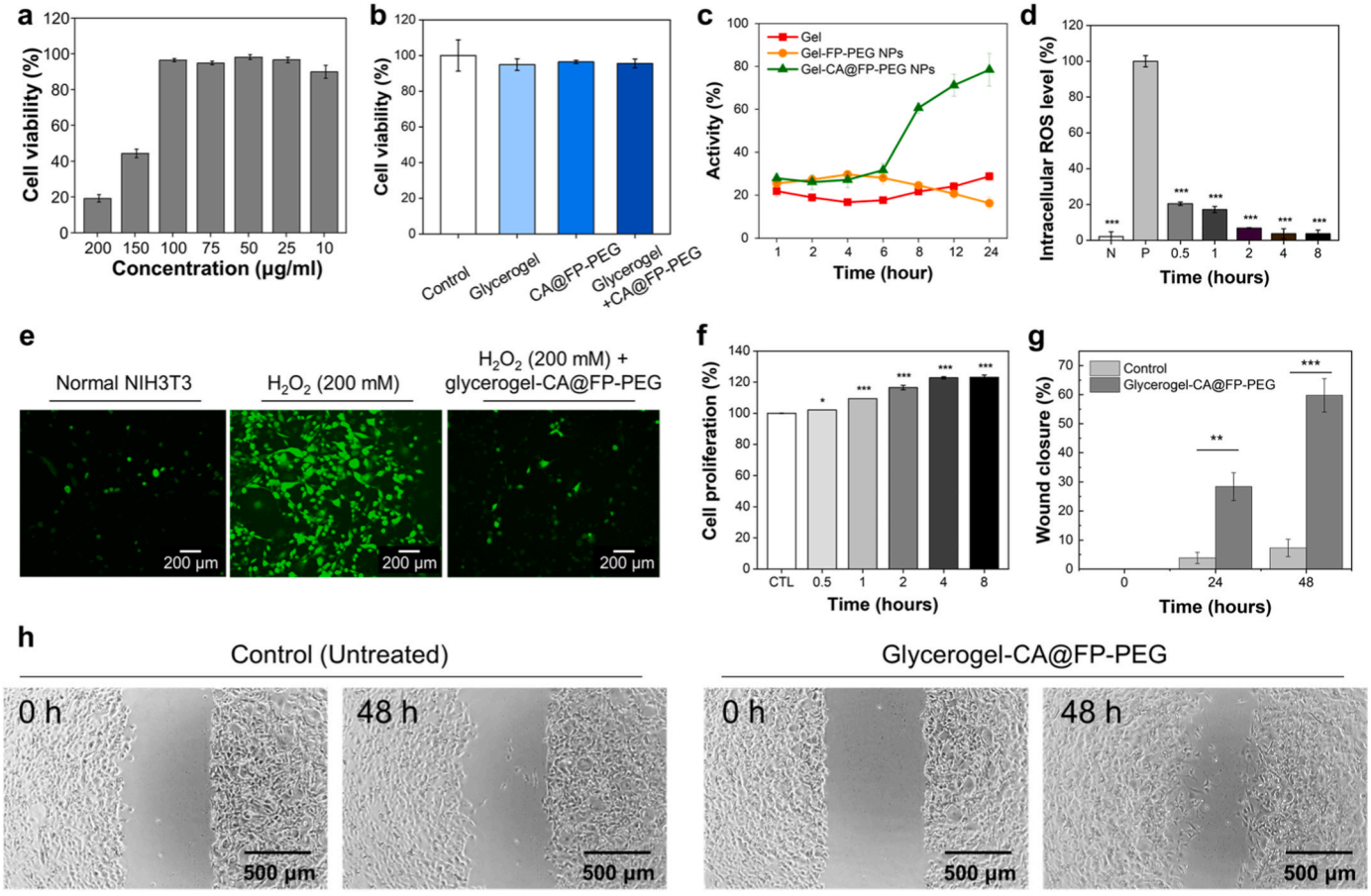

Fig. 5. ***In vitro*** **biocompatibility, antioxidant activity, and wound healing performance of the glycerogel-CA@FP-PEG NP system.** (a) Viabilities of NIH3T3 fibroblasts treated with CA@FP-PEG NPs at concentrations ranging from 0 to 200 μg mL^{-1}. (b) Cytocompatibility of glycerogel, CA@FP-PEG NPs, and glycerogel-CA@FP-PEG NPs evaluated using the CCK-8 assay. (c) DPPH radical scavenging activity of each component over time following exposure to 200 mM H_2O_2. (d) Time-dependent intracellular ROS levels in NIH3T3 cells treated with glycerogel–CA@FP–PEG NPs (H2DCFDA assay), and (e) corresponding representative fluorescence images after 8 h of treatment. (f) NIH3T3 cell proliferation over time after treatment with CA@FP-PEG NPs released from the glycerogel at defined intervals. (g) Quantitative analysis of wound closure in a scratch assay at 24 and 48 h after treatment. (h) Representative microscopic images of scratch wound healing in NIH3T3 monolayers at 0 and 48 h post-treatment. Statistical significance in (d) and (f) were determined relative to the untreated control group. Statistical significance is indicated as $*p < 0.05$, $**p < 0.01$, and $***p < 0.001$.

Glycerogel-CA@FP-PEG NP-treated cells demonstrated a significant decrease in ROS levels from 20.43% at 0.5 h to 3.68% at 8 h post-treatment. This ROS scavenging behavior, as evidenced by time-resolved DPPH radical scavenging and intracellular ROS reduction (Fig. 5c), was closely correlated with the time-dependent CA release (Fig. 2j).

2.8. *In vitro cell proliferation and wound healing activity*

To assess the wound-healing potential of the developed system, fibroblast-based assays and ROS-scavenging analyses were selected as an initial evaluation platform, given the central role of fibroblasts in tissue repair and the importance of oxidative balance in maintaining a pro-regenerative microenvironment [35,36]. Accordingly, we investigated the effects of glycerogel–CA@FP–PEG NPs on fibroblast proliferation and migration, two critical cellular processes involved in wound healing. NIH3T3 cells were treated with CA@FP–PEG NPs released from the glycerogel at defined time intervals (0.5, 1, 2, 4, and 8 h) to simulate time-dependent drug exposure. Importantly, the release samples used for these assays were collected under ROS-free conditions to evaluate the intrinsic pro-regenerative bioactivity of the released nanoparticles without the confounding influence of continuous oxidative stress. Cell proliferation was evaluated using the CCK-8 assay. All treatment groups exhibited increased cell proliferation compared with the untreated control, with the highest level observed at the 8-h release point. At this time, cell proliferation reached 123.11% relative to that of the control (Fig. 5f). Collectively, these results suggest that sustained CA release provides prolonged biological stimulation, supporting fibroblast growth.

To determine whether this enhanced proliferation translated into functional cellular migration, we conducted an *in vitro* scratch wound-healing assay. NIH3T3 monolayers were scratched and treated with CA@FP-PEG NPs released at 8 h, which was selected as a representative condition because it showed the most pronounced proliferative response while remaining consistent with the overall time-dependent biological trend. After 24 h, the treated group exhibited a wound closure rate of 28.4 ± 4.8%, compared with 3.85 ± 1.9% in the untreated control group. After 48 h, wound closure further increased to 59.77 ± 5.77% in the treated group, whereas the untreated control group showed only 7.29 ± 2.98% closure (Fig. 5g and h). Microscopic imaging corroborated these findings, revealing a substantial reduction in the wound gap in the treatment group.

2.9. *In vivo wound healing study*

Full-thickness excisional dorsal wounds were created in 10-week-old male Sprague–Dawley rats (Orient Bio Inc., Seongnam, South Korea) under aseptic conditions. The wound-healing procedure is shown in

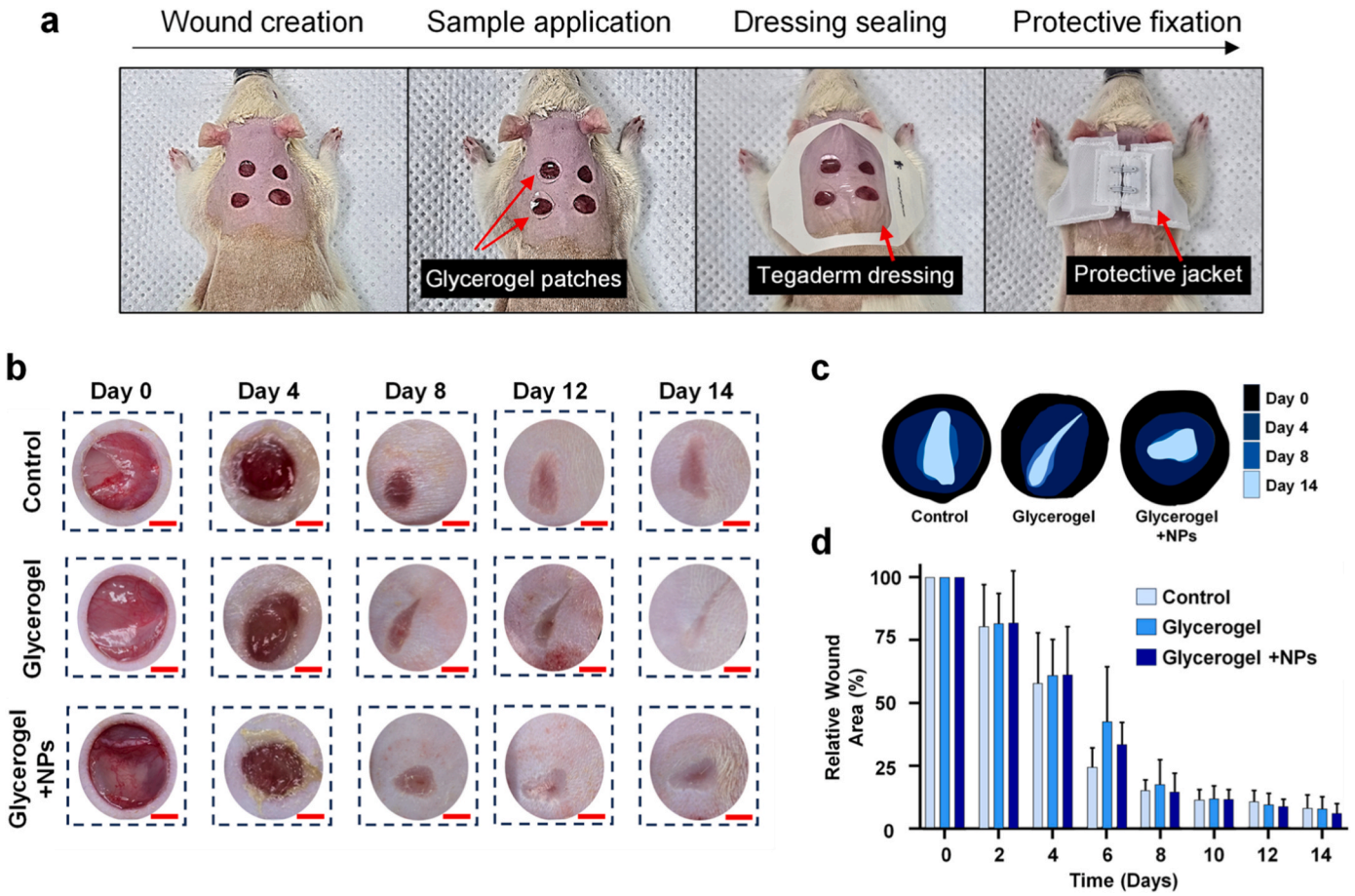

Fig. 6. ***In vivo*** **wound healing performance of glycerogel–CA@FP-PEG NP dressings in a full-thickness rat skin wound model.** (a) Representative photographs of the wound-healing procedure, including application of the samples, coverage with a conventional dressing, and fixation using a protective jacket, followed by monitoring over the designated time period. (b) Representative photographs of wounds at 0, 4, 8, 12, and 14 days post-injury (scale bar = 3 mm). (c) Two-dimensional planimetric reconstructions of wound areas from serial photographs, showing centripetal wound contraction. (d) Quantitative analysis of wound closure over 14 days based on planimetric measurements.

Fig. 6a, including sample application, coverage with a conventional dressing, and fixation using a protective jacket to maintain the dressing during the observation period. The animals were then randomly assigned to three groups: control (no dressing), glycerogel, and glycerogel–CA@FP–PEG NPs. Wound closure was monitored for 14 d by digital planimetry of serial photographs, with wound areas normalized to those on day 0 (Fig. 6a and b).

Serial wound photographs were processed into two-dimensional planimetry for the quantitative assessment of wound area reduction. Consistent with *in vitro* result, the glycerogel-CA@FP-PEG NP group exhibited the most pronounced and symmetric closure pattern (Fig. 6c). Consistently, quantitative wound area analysis confirmed progressive contraction in all groups, reaching > 80% closure by day 14 (control, 80%; glycerogel, 86%; and glycerogel-CA@FP-PEG NPs, 89%) (Fig. 6d).

The glycerogel-CA@FP-PEG NP group exhibited the fastest early-phase closure, achieving approximately 80% contraction by day 8 and maintaining a steady trajectory thereafter. Moreover, contraction in this group was more centrally directed and spatially uniform, reflecting improved epithelial bridging and coordinated tissue remodeling, rather than mere surface area reduction [37]. Overall, these findings suggest that drug incorporation into glycerogels enhances not only the rate but also the quality of wound regeneration.

Hematoxylin and eosin (H&E) staining was performed to examine the structural characteristics of the regenerated skin (Fig. 7a). Although the wounds in the control group appeared nearly closed, they exhibited incomplete re-epithelialization, with tissue discontinuity and persistent inflammatory cell infiltration within the wound bed (Fig. 7a) [38]. In contrast, both glycerogel-treated groups developed a continuous neo-epidermis without apparent disruption or inflammatory infiltration. Among them, the glycerogel-CA@FP-PEG NP group formed a more stratified epidermis with significantly greater thickness (control: 82.9 ± 5.5 μm; glycerogel: 97.3 ± 16.2 μm; glycerogel-CA@FP-PEG NPs: 134.9 ± 38.6 μm), consistent with accelerated epithelial coverage and attenuated inflammation. These results align with previous reports, indicating that ROS modulation supports orderly re-epithelialization and mitigates sustained inflammation in chronic-like wound environments [39,40].

Masson's trichrome (MT) staining was performed to further examine extracellular matrix remodeling (Fig. 7b). Importantly, the control and glycerogel groups exhibited relatively sparse and disorganized collagen fibers, characteristic of immature granulation tissues. In contrast, the glycerogel-CA@FP-PEG NP group exhibited denser and more organized collagen deposition, with fibers aligned in a pattern resembling the normal dermis. This enhanced collagen maturation suggests that the dressing not only accelerates wound closure but also promotes structural regeneration toward a skin-like architecture. Importantly, the presence of well-aligned collagen fibers indicates the potential for improved mechanical integrity and reduced scar formation, which are often critical for the functional restoration of chronic or high-tension wounds. Particularly, the collagen bundles in the glycerogel-CA@FP-PEG NP group appeared to extend inward from both wound margins, forming an organized bridge across the defect, indicative of coordinated dermal

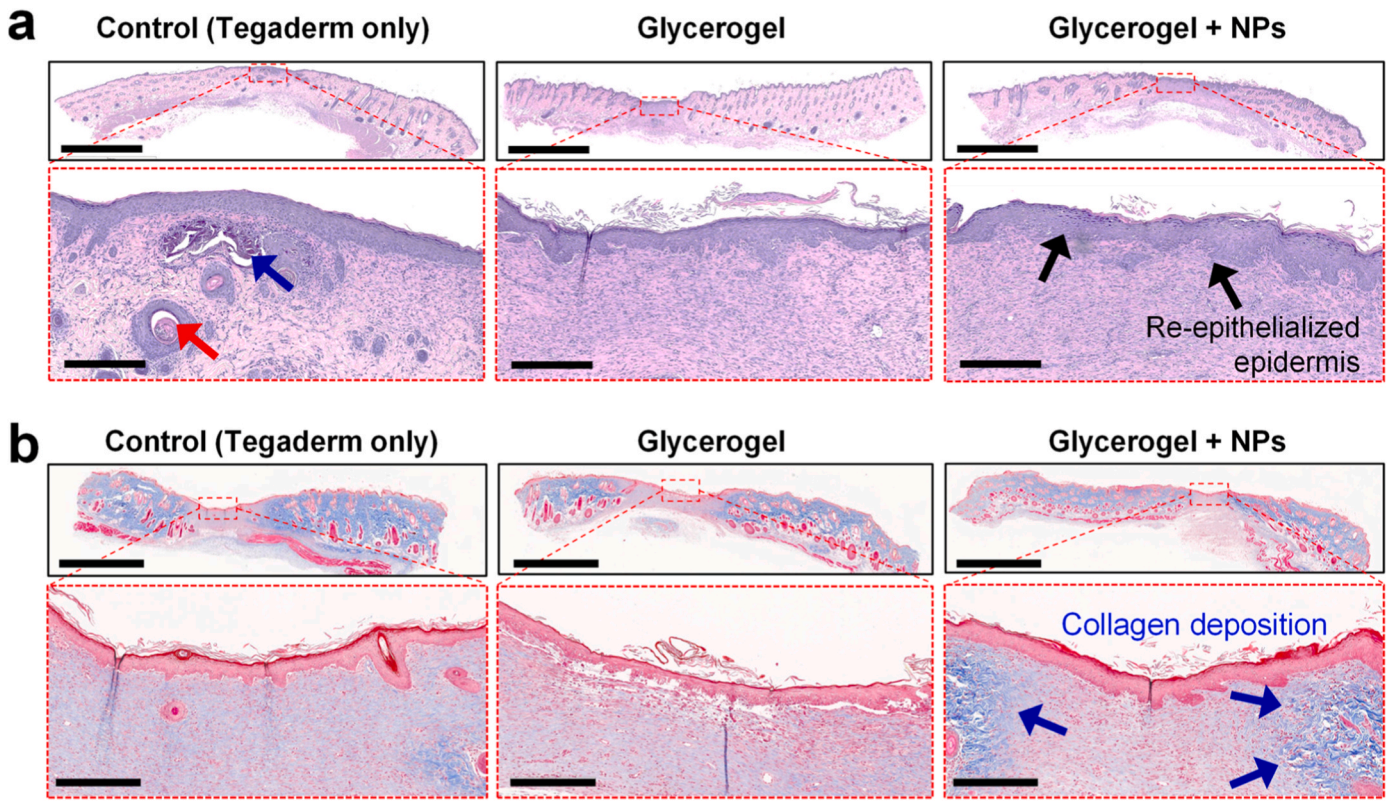

Fig. 7. Histological evaluation of in vivo wound healing in a full-thickness skin wound model in rats. (a) Hematoxylin and eosin-stained tissue sections on day 14. The upper panels (scale bar = 3 mm) show whole tissue sections with rectangular red boxes marking the original wound site. Corresponding magnified images (scale bar = 300 μm) highlight key histological features, including inflammatory cell infiltration (red arrow), tissue disruption (blue arrow), and re-epithelialization (black arrows). (b) Masson's trichrome staining on day 14. Upper panels (scale bar = 3 mm) show whole tissue sections with rectangular red boxes marking the wound region. Enlarged images (scale bar = 300 μm) display collagen deposition, with blue arrows indicating fibrous collagen bundles. (For interpretation of the references to colour in this figure legend, the reader is referred to the Web version of this article.)

remodeling.

Collectively, these findings indicate that the ROS-responsive glycerogel dressing accelerates wound closure and promotes higher-quality tissue regeneration by facilitating epithelial coverage, attenuating inflammation, and guiding organized collagen remodeling. Such outcomes are essential for rapid healing, restoration of skin function, minimization of scar formation, and long-term mechanical stability. Overall, these results underscore the translational potential of the glycerogel–CA@FP–PEG NP system as an advanced therapeutic dressing for chronic, inflammatory, or mechanically stressed wounds, where both the speed and quality of repair are critical. Nevertheless, further studies incorporating direct ROS measurement, vascularization analysis, and pathological wound models will be necessary to more fully define the mechanistic advantages of this ROS-responsive platform.

3. Conclusions

A multifunctional wound dressing that combines a tough glycerogel matrix with ROS-responsive drug-loaded ferrocene NPs was developed. Mechanical robustness was achieved through polymer entanglement in a single acrylamide hydrogel formulation, and solvent exchange with a water–glycerol mixture imparted long-term hydration and enhanced bioadhesion. Additionally, the embedded NPs enabled redox-triggered CA release, providing dynamic antioxidant therapy in oxidative wound environments. Comprehensive evaluations demonstrated that this multifunctional dressing promoted fibroblast proliferation, migration, and ROS scavenging *in vitro* and accelerated wound closure, enhanced re-epithelialization, reduced inflammation, and guided collagen remodeling toward a skin-like architecture in vivo. In addition to facilitating wound contraction, the dressing restored both the structural integrity and functional quality of the regenerated skin, underscoring its potential for treating chronic, inflammatory, and mechanically stressed wounds. This study introduces a broadly applicable strategy for next-generation hydrogel dressings that integrate resilience, adhesiveness, and smart therapeutic delivery systems.

4. Materials and methods

4.1. Materials

FMMA (95%) was obtained from Aaron Pharmatech Ltd., China. MA (99%) and PEGMA (Mn = 500 g mol^{-1}, 99%) were purchased from Merck, Germany, and passed through inhibitor removal columns before use. 2,2′-Azobis(2-methylpropionitrile) (AIBN, 99%; Junsei Chemical, Japan) was recrystallized from methanol (MeOH, 99.8%; Daejung Chemicals & Metals Co., Ltd., South Korea). Deionized (DI) water and phosphate-buffered saline (PBS) were purchased from Merck, Germany. CA, acrylamide (AAm), N,N′-methylenebisacrylamide (BIS), N,N,N′,N′-tetramethylethylenediamine (TEMED), tetrahydrofuran (THF, 99.9%), dimethyl sulfoxide-d6 (DMSO-d6, 99.9%), and ammonium persulfate (APS) were obtained from Sigma-Aldrich (USA). Glycerol (99.8%) was purchased from Samchun Chemical, South Korea. For *in vitro* cell culture, Dulbecco's modified Eagle's medium (DMEM), penicillin-streptomycin (PS), and fetal bovine serum (FBS) were purchased from Gibco, USA. H2DCFDA was purchased from Invitrogen, USA.

4.2. Synthesis and characterization of FP

FP and FP-PEG were synthesized by free-radical polymerization using FMMA, MA, and PEGMA to improve drug-loading efficiency and

water dispersibility. MA and PEGMA were purified using inhibitor removal columns for 1 h before use. FP was synthesized from MA (2 mmol) and FMMA (0.4 mmol), whereas FP-PEG was synthesized from MA (1 mmol), FMMA (0.4 mmol), and PEGMA (1 mmol). AIBN (0.12 mmol) was used as the radical initiator and dissolved in 14 mL of THF. After degassing with argon for 10 min, the reaction mixture was sealed and stirred at 70 °C in an oil bath for 24 h. The resulting polymer solution (10 wt%) was cooled to 25 °C and stored at 4 °C. The polymer was purified by precipitation in hexane three times and dried in a vacuum oven at 25 °C for 24 h. The chemical structure was confirmed by ˆ1H NMR spectroscopy (400 MHz, DMSO-d6, 25 °C; JNM-ECZ400S/L1, JEOL, Japan). Mw, Mn, and PDI (Mw/Mn) were determined by GPC in THF at a flow rate of 1 mL min^{-1} and 35 °C using a refractive-index detector.

4.3. Preparation and characterization of CA@FP–PEG NPs

CA@FP-PEG NPs were prepared by nanoprecipitation. The drug-loading performance of FP and FP-PEG was first evaluated using 10 wt % CA relative to the polymer. Each polymer solution (50 μL, 10 wt% in THF) was mixed with 1 mg of CA and stirred for 2 h, and the mixture was then added dropwise to 5 mL of DI water through a 30 G syringe under constant stirring at 530 rpm. THF was evaporated in a fume hood for 12 h. The hydrodynamic diameter and zeta potential of the particles were measured by DLS (ELSZ-2000; Otsuka Electronics, Japan). FP-PEG was selected as the carrier for subsequent studies. CA@FP-PEG NPs containing 0, 10, 20, and 40 wt% CA were prepared and analyzed for size, dispersity, and morphology over 4 weeks. Particle morphology was further examined by TEM. Redispersibility was assessed after lyophilization for 3 d without a cryoprotectant, followed by rehydration in biological buffer (1.2 mg mL^{-1}).

4.4. Evaluation of stability and ROS-responsive property of CA@FP-PEG NPs

To evaluate ROS responsiveness, CA@FP-PEG NPs were incubated with 200 mM H_2O_2. DLS measurements were obtained at 0.5, 2, 4, 6, 8, 12, 24, and 48 h, and TEM images were acquired after 6 h of incubation. For the release study, purified CA@FP-PEG NPs were incubated in H_2O_2-containing buffer at 37 °C and 100 rpm for 48 h. The particles were purified using an Amicon Ultra-15 centrifugal filter (100 kDa cutoff; MilliporeSigma, USA), and the release medium was replaced at designated time points. CA concentration was quantified by HPLC using a C18 column (5 μm, 4.6 × 150 mm; SunFire® C18, Waters, USA). The mobile phase consisted of 80% water and 20% ACN, and the analysis time was 30 min. Unloaded CA was quantified by UV-Vis spectroscopy at 220 nm. Drug loading content (LC) and loading efficiency (LE) were calculated using the following equations:

$$\mathrm{LC}\ (\%) = \frac{\textit{weight of fed drug} - \textit{weight of unloaded drug}}{\textit{weight of FP} - \textit{PEG NPs}} \times 100 \quad (1)$$

$$\mathrm{LE}\ (\%) = \frac{\textit{weight of fed drug} - \textit{weight of unloaded drug}}{\textit{weight of fed drug}} \times 100 \quad (2)$$

4.5. Fabrication of glycerogel loaded with CA@FP-PEG NPs

A mechanically robust hydrogel was prepared by mixing 40 μL of 2 wt% BIS, 100 μL of 10 wt% APS, and 10 mL of 40 wt% AAm, followed by the addition of 1 μL of TEMED. The molar ratios of initiator and cross-linker to monomer were 1:63 and 1:10,800, respectively. The precursor solution was quickly poured between two glass plates separated by a 1 mm gap. The resulting hydrogel was washed with DI water to remove unreacted monomers and then dried to obtain the tough hydrogel. Glycerogels were prepared by re-swelling the dried hydrogel in glycerol-water mixtures with G/W volume ratios of 0, 0.1, 0.2, 0.5, and 1.0. CA@FP-PEG NP-loaded glycerogels were prepared by adding CA@FP-PEG NPs to the glycerol-water mixture during the re-swelling step. All CA@FP–PEG nanoparticle solutions were prepared at a fixed concentration of 0.5 g L^{-1}, defined as the loading-bath concentration used during glycerogel fabrication. Glycerogel samples were immersed in this solution to allow nanoparticle uptake, and the absorbed amount was estimated from the concentration difference in the loading solution before and after swelling.

4.6. Equilibrium swelling ratio (ESR) of glycerogel–CA@FP–PEG NPs

The contents of mixture and polymer in glycerogel and glycerogel-CA@FP-PEG NPs were quantified by TGA (SDT Q 600; TA Instruments, USA). Water and glycerol contents were determined from the mass loss over the ranges of 25-110 °C and 110-300 °C, respectively. The polymer mass was taken as the remaining mass. The ESR values of the mixture and water were calculated using the following equation:

$$\mathrm{ESR}\ (\%) = \frac{\textit{weight of mixture}}{\textit{weight of gel polymer}} \times 100 \quad (3)$$

4.7. Water retention in glycerogel-CA@FP-PEG NPs

All glycerogels and glycerogel-CA@FP-PEG NPs were prepared as disks with a diameter of 2.54 cm and thickness of 1 mm after complete swelling in a mixture of glycerol and water under each condition. After removing unabsorbed liquid on the gel surface using sterile tissue, the samples were weighed. Thereafter, the samples were dried at an average relative humidity of 35% – 40% for 30 d and weighed at various time points. Normalized mass was recorded as the weight of the gel at a given time divided by the initial weight of the gel.

4.8. Visualization and quantification of FP-PEG NPs in glycerogel

To visualize NP incorporation into the hydrogel matrix, Nile Red-loaded FP-PEG NPs (NR@FP-PEG NPs) were prepared. Dried hydrogels were re-swollen in NR@FP-PEG NP solution to obtain glycerogel-NR@FP-PEG NPs. Light exposure was minimized during preparation to prevent photooxidation of Nile Red. Fluorescence images were acquired using confocal laser scanning microscopy (LSM980 with Airyscan2; Carl Zeiss, Germany) at an excitation wavelength of 520 nm. The loading amount of CA@FP-PEG NPs in glycerogel-CA@FP-PEG NPs was quantified from the difference in NP concentration in the swelling solution before and after gel rehydration. The volume of NP solution absorbed by the gel was determined from the weight difference before and after complete swelling. FP-PEG NPs were quantified by UV-Vis spectroscopy (Mega900; SCINCO Co., Ltd., South Korea) at approximately 285 nm.

4.9. CA@FP-PEG NP stability in glycerol and water mixtures at various ratios

To assess the stability of CA@FP-PEG NPs in glycerol-water mixtures, hydrodynamic diameters were measured by DLS. CA@FP-PEG NPs were dispersed in mixtures with G/W volume ratios of 0, 0.1, 0.2, 0.5, and 1.0, and particle diameters were monitored over 30 d at designated time points.

4.10. Adhesive strength and mechanical properties

Adhesive and mechanical properties were measured using a universal testing machine (Z050; ZwickRoell GmbH & Co., Germany) equipped with a 100 N load cell. Adhesive performance was evaluated by lap shear, tensile adhesion, and cyclic adhesion tests using glycerogel and glycerogel–CA@FP–PEG NPs. For lap shear tests, porcine skin substrates were prepared in strips of 40 × 80 × 0.5 mm, and the bonded

area was fixed at 40 × 40 mm. For tensile adhesion tests, square porcine skin substrates (40 × 40 × 0.5 mm) were used with the same bonded area. In both tests, samples were pulled at 100 mm min^{-1} until complete separation, and adhesion strength was calculated by dividing the maximum load by the bonded area. Porcine skin was soaked in PBS at 4 °C for at least 3 d before use. Cyclic adhesion was evaluated for 30 attachment-detachment cycles using the tensile adhesion configuration. To assess the intrinsic mechanical properties of the gels, tensile tests were additionally performed using gel specimens with dimensions of 20 × 40 × 0.5 mm. The initial grip separation was 20 mm, and the tensile rate was 10 mm min^{-1} until fracture.

Ex vivo tissue adhesion tests were performed using freshly excised liver, kidney, and skin tissues from Sprague–Dawley rats. The tissues were rinsed with phosphate-buffered saline (PBS) and used immediately. A predefined amount of glycerogel was applied to the tissue surface and gently pressed to ensure conformal contact. After a short equilibration period (~10 s), adhesion was qualitatively evaluated by manual lifting to assess whether the glycerogel remained attached without detachment. Representative images were recorded under ambient conditions using a digital camera.

4.11. CA@FP-PEG NP release from glycerogel-CA@FP-PEG NPs

The release of CA@FP-PEG NPs from glycerogel-CA@FP-PEG NPs was quantified by measuring NP concentrations in PBS at 0.5, 1, 2, 4, 6, 8, 12, and 24 h. Samples were immersed in 10 mL of PBS at room temperature, and the NP concentration in the release medium at each time point was analyzed by UV-Vis spectroscopy at 285 nm. Three independent samples were used for each condition.

4.12. In vitro cytotoxicity of glycerogel-CA@FP-PEG NPs

Cytocompatibility of CA@FP–PEG nanoparticles was first evaluated in NIH3T3 mouse embryonic fibroblasts over a concentration range of 0–200 μg mL^{-1}, defined as the biological exposure concentration in cell culture. Cell viability remained above 95% up to 100 μg mL^{-1}, indicating negligible cytotoxicity within the therapeutically relevant range. For comparative evaluation of the individual components and the final formulation, NIH3T3 cells were seeded in 96-well plates at 1×10^4 cells per well in DMEM supplemented with 10% FBS and 1% penicillin-streptomycin, and cultured for 24 h at 37 °C. The cells were then treated for 24 h with glycerogel, CA@FP–PEG NPs, or glycerogel–CA@FP–PEG NPs. For the NP treatment group, CA@FP–PEG NPs were applied at a maximum concentration of 27 μg mL^{-1}, corresponding to the highest amount released from glycerogel–CA@FP–PEG NPs. CCK-8 solution diluted to 10% in DMEM was added to each well and incubated for 1 h. Absorbance at 450 nm was measured using a microplate reader (BioTek Instruments, Winooski, VT, USA). Cell viability was calculated as follows:

$$\text{Cell viability}(\%) = \frac{\Delta A_{450}\ of\ test\ group}{\Delta A_{450}\ of\ control\ group} \quad (4)$$

4.13. DPPH radical-scavenging assay

The free radical-scavenging activities of glycerogel, FP-PEG NPs, and CA@FP-PEG NPs were evaluated using a DPPH assay. A 1 mM DPPH solution in ethanol was prepared and stored at 4 °C in the dark. Then, 150 μL of DPPH solution was mixed with 150 μL of each aqueous sample solution. A mixture of 150 μL DPPH solution and 150 μL DI water was used as the control. All mixtures were incubated for 30 min at room temperature in the dark, and absorbance was measured at 515 nm using a microplate reader. Antioxidant activity was calculated using the following equation:

$$\text{Antioxidant activity}\ (\%) = \left[\frac{(\Delta A_{515}\ \text{of control} - \Delta A_{515}\ \text{of sample})}{\Delta A_{515}\ \text{of control}}\right] \times 100$$

4.14. In vitro ROS scavenging effect of glycerogel-CA@FP-PEG NPs

NIH3T3 cells were seeded in 96-well plates at 1×10^4 cells per well and cultured for 24 h. CA@FP–PEG NPs released from glycerogel–CA@FP–PEG NPs were collected at hourly intervals from 0.5 to 8 h and applied to the cells. Oxidative stress was then induced by treatment with 50 μM H_2O_2 for 4 h. A negative control group was prepared without H_2O_2 treatment. After washing with PBS, the cells were incubated with 10 μM H2DCFDA for 90 min in the dark. Intracellular ROS levels were quantified by measuring the fluorescence intensity of oxidized dichlorofluorescein at excitation/emission wavelengths of 485/535 nm using a microplate reader.

4.15. Cell proliferation and wound healing ability of glycerogel-CA@FP-PEG NPs

For the proliferation assay, NIH3T3 cells were seeded in 96-well plates at 1×10^4 cells per well and cultured for 24 h. The cells were then incubated in serum-free medium for 4 h, during which CA@FP–PEG NPs released hourly (0.5-8 h) from glycerogel–CA@FP–PEG NPs were added. After 24 h, CCK-8 solution was added and incubated for 1 h, and absorbance was measured at 450 nm using a microplate reader (BioTek Instruments).

For the scratch wound-healing assay, NIH3T3 cells were seeded in 24-well plates at 2×10^5 cells per well and cultured for 24 h. A linear scratch was created using a sterile P1000 pipette tip, and the wells were washed with DMEM to remove detached cells and debris. Cells were then treated with 27 μg mL^{-1} CA@FP–PEG NPs, corresponding to the maximum concentration released from glycerogel–CA@FP–PEG NPs. The control group received serum-free DMEM only. Wound closure was monitored for 48 h using a DMi1 light microscope (Leica Microsystems, Wetzlar, Germany) at × 4 magnification and quantified using ImageJ software (version 1.8.0; NIH, Bethesda, MD, USA).

4.16. Wound healing assessment in vivo

Ten-week-old male Sprague-Dawley rats (Orient Bio Inc.) were used to evaluate the wound-healing efficacy of the drug-loaded glycerogel formulation. Animals were acclimatized for 1 week at the Preclinical Resource Center of Samsung Medical Center (South Korea). All animal procedures were approved by the Institutional Animal Care and Use Committee of Samsung Medical Center (Approval No. 20241224009). Under anesthesia, three evenly spaced full-thickness excisional wounds (8 mm in diameter) were created on the shaved and sterilized dorsal skin of each rat using sterile biopsy punches. The wounds were assigned to one of three treatment groups: control, glycerogel, and glycerogel–CA@FP–PEG NPs. Circular patches (12 mm in diameter) were applied to cover the wound area. To maintain the dressings throughout the healing period, a transparent film dressing (Tegaderm 1624W, 3M, USA) was applied over each patch, followed by a silicone pad to minimize displacement. The dressings were then secured using a rat jacket. Patches and coverings were replaced every 2 d for 14 d, and the dressings were temporarily removed during each exchange for wound imaging. Digital photographs were obtained on days 0, 4, 8, 12, and 14, and wound areas were quantified using ImageJ software (NIH). On day 14, wound-margin tissues were harvested for histological analysis.

4.17. H&E staining

Paraffin-embedded tissue sections were deparaffinized in xylene for 20 min and rehydrated through a graded ethanol series (100, 95, 80, and

75%). After rinsing with distilled water, the sections were stained with hematoxylin for 5 min, washed under running tap water, and counter-stained with eosin for 2 min. The sections were then dehydrated in absolute ethanol, cleared in xylene for 15 min, and mounted with neutral resin and coverslips. Images were acquired using a digital slide scanner (Aperio AT2; Leica Biosystems, Germany) at × 40 magnification, and epidermal thickness was quantified using ImageJ software (NIH).

4.18. MT staining

For MT staining, sections were deparaffinized and rehydrated as described above. Staining was performed using a commercial kit (Trichrome Stain Kit Masson; StatLab Medical Products, USA) according to the manufacturer's instructions. Briefly, sections were treated with Weigert's iron hematoxylin for 10 min, differentiated, and sequentially stained with ponceau-acid fuchsin, phosphomolybdic acid, and aniline blue. After treatment with 1% glacial acetic acid, the sections were dehydrated, cleared, and mounted. Images were acquired at × 40 and × 100 magnification using an Aperio AT2 system (Leica Biosystems, Germany).

CRediT authorship contribution statement

Jiwon Kang: Writing – original draft, Methodology, Formal analysis, Data curation. **Sohyun Yu:** Writing – original draft, Methodology, Investigation, Formal analysis, Data curation. **Jisu Kim:** Methodology, Investigation, Formal analysis, Data curation. **Seongwoo Yang:** Writing – original draft, Methodology, Formal analysis, Data curation. **Won Il Choi:** Writing – review & editing. **Jinhan Cho:** Writing – review & editing, Supervision. **Jeonghun Kim:** Writing – review & editing, Writing – original draft, Methodology, Investigation. **Daekyung Sung:** Writing – review & editing, Writing – original draft, Conceptualization. **Byoung Soo Kim:** Writing – review & editing, Writing – original draft, Supervision, Project administration, Methodology, Conceptualization.

Funding sources

This work was supported by the Korea Health Technology R&D Project through the Korea Health Industry Development Institute (KHIDI), funded by the Ministry of Health & Welfare (HP23C0040), the Korea Institute of Ceramic Engineering and Technology (KICET) (2410013749), and the Ministry of SMEs and Startups (MSS, Korea) (RS-2025-02314914) to B.S. Kim.

Declaration of competing interest

The authors declare the following financial interests/personal relationships which may be considered as potential competing interests: Byoung Soo Kim reports financial support was provided by Korea Health Industry Development Institute. Byoung Soo Kim reports financial support was provided by Korea Institute of Ceramic Engineering and Technology. If there are other authors, they declare that they have no known competing financial interests or personal relationships that could have appeared to influence the work reported in this paper.

Appendix A. Supplementary data

Supplementary data related to this article can be found online at https://doi.org/10.1016/j.mtadv.2026.100774.

Data availability

Data will be made available on request.

References

[1] D. Queen, H. Orsted, H. Sanada, G. Sussman, A dressing history, Int. Wound J. 1 (2004) 59–77, https://doi.org/10.1111/j.1742-4801.2004.0009.x.
[2] G.D. Winter, J.T. Scales, Effect of air drying and dressings on the surface of a wound, Nature 197 (1963) 91–92, https://doi.org/10.1038/197091b0.
[3] H.M. Nguyen, T.T.N. Le, A.T. Nguyen, H.N.T. Le, T.T. Pham, Biomedical materials for wound dressing: recent advances and applications, RSC Adv. 13 (2023) 5509–5528, https://doi.org/10.1039/D2RA07673J.
[4] S. Dhivya, V.V. Padma, E. Santhini, Wound dressings–a review, Biomedicine 5 (2015) 22, https://doi.org/10.7603/s40681-015-0022-9.
[5] Y. Dong, Z. Wang, ROS-scavenging materials for skin wound healing: advancements and applications, Front. Bioeng. Biotechnol. 11 (2023) 1304835, https://doi.org/10.3389/fbioe.2023.1304835.
[6] M. Hunt, M. Torres, E. Bachar-Wikstrom, J.D. Wikstrom, Cellular and molecular roles of reactive oxygen species in wound healing, Commun. Biol. 7 (2024) 1534, https://doi.org/10.1038/s42003-024-07219-w.
[7] W. Yu, Y. Tu, Z. Long, J. Liu, D. Kong, J. Peng, C. Hai, Reactive oxygen species bridge the gap between chronic inflammation and tumor development, Oxid. Med. Cell. Longev. 2022 (2022) 2606928, https://doi.org/10.1155/2022/2606928.
[8] H. Kaur, B. Gogoi, I. Sharma, D.K. Das, M.A. Azad, D.D. Pramanik, A. Pramanik, Hydrogels as a potential biomaterial for multimodal therapeutic applications, Mol. Pharm. 21 (2024) 4827–4848, https://doi.org/10.1021/acs.molpharmaceut.4c00595.
[9] M. Ribeiro, M. Simões, C. Vitorino, F. Mascarenhas-Melo, Hydrogels in cutaneous wound healing: insights into characterization, properties, formulation and therapeutic potential, Gels 10 (2024) 188, https://doi.org/10.3390/gels10030188.
[10] E. Rezvani Ghomi, S. Khalili, S. Nouri Khorasani, R. Esmaeely Neisiany, S. Ramakrishna, Wound dressings: current advances and future directions, J. Appl. Polym. Sci. 136 (2019) 47738, https://doi.org/10.1002/app.47738.
[11] T. Billiet, M. Vandenhaute, J. Schelfhout, S. Van Vlierberghe, P. Dubruel, A review of trends and limitations in hydrogel-rapid prototyping for tissue engineering, Biomaterials 33 (2012) 6020–6041, https://doi.org/10.1016/j.biomaterials.2012.04.050.
[12] X. Liu, S. Qin, L. Xu, G. Fu, Y. Huang, C. Yu, D. Sun, A tough and mechanically stable adhesive hydrogel for non-invasive wound repair, Front. Bioeng. Biotechnol. 11 (2023) 1173247, https://doi.org/10.3389/fbioe.2023.1173247.
[13] Y. Seo, B.S. Kim, W.C. Ballance, N. Aw, B. Sutton, H. Kong, Transparent and flexible electronics assembled with metallic nanowire-layered nondrying glycerogel, ACS Appl. Mater. Interfaces 12 (2020) 13040–13050, https://doi.org/10.1021/acsami.9b21697.
[14] W. Zhang, S. Chen, W. Jiang, Q. Zhang, N. Liu, Z. Wang, D. Zhang, Double-network hydrogels for biomaterials: structure-property relationships and drug delivery, Eur. Polym. J. 185 (2023) 111807, https://doi.org/10.1016/j.eurpolymj.2022.111807.
[15] H. Xin, Double-network tough hydrogels: a brief review on achievements and challenges, Gels 8 (2022) 247, https://doi.org/10.3390/gels8040247.
[16] S. Wang, J. Li, Y. Pan, F. Liu, L. Zeng, Y. Gao, T. Lu, A double-network strategy for the tough tissue adhesion of hydrogels with long-term stability under physiological environment, Soft Matter 18 (2022) 6192–6199, https://doi.org/10.1039/D2SM00688J.
[17] J. Li, D.J. Mooney, Designing hydrogels for controlled drug delivery, Nat. Rev. Mater. 1 (2016) 16071, https://doi.org/10.1038/natrevmats.2016.71.
[18] J.Y. Seo, B. Lee, T.W. Kang, J.H. Noh, M.J. Kim, Y.B. Ji, M.S. Kim, Electrostatically interactive injectable hydrogels for drug delivery, Tissue Eng. Regen. Med. 15 (2018) 513–520, https://doi.org/10.1007/s13770-018-0146-6.
[19] L. Fabbrizzi, The ferrocenium/ferrocene couple: a versatile redox switch, ChemTexts 6 (2020) 1–20, https://doi.org/10.1007/s40828-020-00119-6.
[20] Y. Na, J.S. Lee, J. Woo, S. Ahn, E. Lee, W.I. Choi, D. Sung, Reactive oxygen species (ROS)-responsive ferrocene-polymer-based nanoparticles for controlled release of drugs, J. Mater. Chem. B 8 (2020) 1906–1913, https://doi.org/10.1039/C9TB02533B.
[21] F. Pittella, R.C. Dutra, D.D. Junior, M.T. Lopes, N.R. Barbosa, Antioxidant and cytotoxic activities of Centella asiatica (L.) Urb, Int. J. Mol. Sci. 10 (2009) 3713–3721, https://doi.org/10.3390/ijms10093713.
[22] B.S. Kim, Y.-H. Deng, J.H. Kim, S.Y. Kim, U. Nwabara, K. Kim, X. Su, H. Kong, Ambient-stable and resilient glycerogel electrolytes for flexible solid-state supercapacitors, ACS Appl. Mater. Interfaces 18 (1) (2026) 1454–1462, https://doi.org/10.1021/acsami.5c19785.
[23] S.Y. Kim, J.-W. Kang, E.H. Jeong, T. Kim, H.L. Jung, J.-U. Park, J. Cho, J.D. Park, B. S. Kim, Synthesis of bioadhesive PHEA hydrogels without crosslinkers through in situ polymerization and sustained mechanical mixing, Korea Aust. Rheol. J. 36 (2024) 71–78, https://doi.org/10.1007/s13367-023-00084-9.
[24] H. Oh, E. Jeong, J.S. Lee, J. Kim, D. Lee, B.S. Kim, D. Sung, H. Koo, W.I. Choi, G. Tae, ROS-responsive pegylated ferrocene polymer nanoparticles with improved stability for tumor-selective chemotherapy and imaging, Mater. Today Bio 22 (2023) 100774, https://doi.org/10.1016/j.mtbio.2023.100774.
[25] P.K. Kandel, L.P. Fernando, P.C. Ackroyd, K.A. Christensen, Incorporating functionalized polyethylene glycol lipids into reprecipitated conjugated polymer nanoparticles for bioconjugation and targeted labeling of cells, Nanoscale 3 (2011) 1037–1045, https://doi.org/10.1039/C0NR00746C.
[26] P.-D. Ly, K.-N. Ly, H.-L. Phan, H.H.T. Nguyen, V.-A. Duong, H.V. Nguyen, Recent advances in surface decoration of nanoparticles in drug delivery, Front. Nanotechnol. 6 (2024) 1456939, https://doi.org/10.3389/fnano.2024.1456939.
[27] G. Zhu, Q. Wang, S. Lu, Y. Niu, Hydrogen peroxide: a potential wound therapeutic target? Med. Princ. Pract. 26 (2017) 301–308, https://doi.org/10.1159/000475501.

[28] A. van der Vliet, Y.M.W. Janssen-Heininger, Hydrogen peroxide as a damage signal in tissue injury and inflammation: Murderer, mediator, or messenger? J. Cell. Biochem. 115 (2014) 427–435, https://doi.org/10.1002/jcb.24683.
[29] W.C. Ballance, V. Karthikeyan, I. Oh, E.C. Qin, Y. Seo, T. Spearman-White, R. Bashir, Y. Hu, H. Phillips, H. Kong, Preoperative vascular surgery model using a single polymer tough hydrogel with controllable elastic moduli, Soft Matter 16 (2020) 8057–8068, https://doi.org/10.1039/D0SM00981D.
[30] I. Munir, G. Yesiloz, Novel size-tunable and straightforward ultra-small nanoparticle synthesis in a varying concentration range of glycerol as a green reducing solvent, ACS Omega 8 (2023) 28456–28466, https://doi.org/10.1021/acsomega.3c02697.
[31] X. Cui, C. Wang, W. Huang, S. Zhang, H. Chen, B. Wu, D. Qin, X. Zheng, Multiple hydrogen bonding-assisted high-strength hydrogel of silica/polyacrylamide nanocomposite cross-linked with polyethylenimine, ACS Omega 8 (2023) 39401–39407, https://doi.org/10.1021/acsomega.3c05025.
[32] Q. Yang, Y. Zhang, Z. Yu, K. Lv, Y. Ye, J. Zhou, N. Lin, Mechanical enhancements and structural simulation of reactive poly(ethylene glycol) and cellulose nanocrystals to polyacrylamide hydrogels, Int. J. Biol. Macromol. 321 (2025) 146494, https://doi.org/10.1016/j.ijbiomac.2025.146494.
[33] J. Zhu, H. Zhou, E.M. Gerhard, S. Zhang, F.I. Parra Rodríguez, T. Pan, H. Yang, Y. Lin, J. Yang, H. Cheng, Smart bioadhesives for wound healing and closure, Bioact. Mater. 19 (2023) 360–375, https://doi.org/10.1016/j.bioactmat.2022.04.020.
[34] H. Ren, Z. Zhang, X. Cheng, Z. Zou, X. Chen, C. He, Injectable, self-healing hydrogel adhesives with firm tissue adhesion and on-demand biodegradation for sutureless wound closure, Sci. Adv. 9 (2023), https://doi.org/10.1126/sciadv.adh4327 eadh4327.
[35] G.C. Gurtner, S. Werner, Y. Barrandon, M.T. Longaker, Wound repair and regeneration, Nature 453 (2008) 314–321, https://doi.org/10.1038/nature07039.
[36] S.A. Eming, P. Martin, M. Tomic-Canic, Wound repair and regeneration: mechanisms, signaling, and translation, Sci. Transl. Med. 6 (2014), https://doi.org/10.1126/scitranslmed.3009337, 265sr6.
[37] Q. Dong, D. Zu, L. Kong, S. Chen, J. Yao, J. Lin, L. Lu, B. Wu, B. Fang, Construction of antibacterial nano-silver embedded bioactive hydrogel to repair infectious skin defects, Biomater. Res. 26 (2022) 36, https://doi.org/10.1186/s40824-022-00281-7.
[38] L. Xu, W. Wei, Q. Jin, W. Ju, X. Wang, C. Xu, Z. Liu, P. Ji, J. Wan, S. Yu, T. Du, Y. Le, Y. Fu, J. Ju, R. Hou, Injectable SilMA-GelMA hybrid hydrogel: a photocurable biomaterial for enhanced wound healing with superior adhesion and biocompatibility, Mater. Today Commun. 44 (2025) 112091, https://doi.org/10.1016/j.mtcomm.2025.112091.
[39] F. Zhang, H. Zhang, S. Wang, M. Gao, K. Du, X. Chen, Y. Lu, Q. Hu, A. Du, S. Du, J. Wang, K. Shi, Z. Chen, Z. Li, Z. Li, J. Xiao, A dynamically phase-adaptive regulating hydrogel promotes ultrafast anti-fibrotic wound healing, Nat. Commun. 16 (2025) 3738, https://doi.org/10.1038/s41467-025-58987-w.
[40] C. Geng, S. He, S. Yu, H.M. Johnson, H. Shi, Y. Chen, Y.K. Chan, W. He, M. Qin, X. Li, Y. Deng, Achieving clearance of drug-resistant bacterial infection and rapid cutaneous wound regeneration using an ROS-balancing-engineered heterojunction, Adv. Mater. 36 (2024) e2310599, https://doi.org/10.1002/adma.202310599.